

# A 10 cm spatial resolution distributed acoustic sensor based on ultra low-loss enhanced backscattering fibre

ALI MASOUDI\*, TIMOTHY LEE, MARTYNAS BERESNA, AND GILBERTO BRAMBILLA

*Optoelectronics Research Centre, University of Southampton, Southampton, SO17 1BJ, UK*

\*[a.masoudi@soton.ac.uk](mailto:a.masoudi@soton.ac.uk)

**Abstract:** In this work, a distributed acoustic sensor (DAS) with 10 cm spatial resolution is demonstrated. Such a high resolution is achieved by employing an ultra low-loss enhanced backscattering (ULEB) fibre as a sensing element. A conventional DAS system is modified to interrogate the ULEB fibre comprised of 50 discrete reflectors with an average reflectance of  $-56$  dB. The ULEB fibre was fabricated with an automated reel-to-reel inscription machine, modified to create more uniform reflectors with similar reflectivity in the core of the fibre. The sensing arrangement exhibits a phase noise of  $1.9 n\epsilon/\sqrt{Hz}$  over 1 km sensing range.

© 2022 Optica Publishing Group

## 1. Introduction

The past decade has witnessed a rapid adoption of distributed acoustic sensor (DAS) technology in various fields from geophysical sciences [1–3] and railway track behavior analysis [4] to hydrocarbon reservoir monitoring [5, 6] and submarine power cable condition assessment [7, 8]. Thus far, most of the research efforts in DAS technology have been devoted to addressing the requirements of the oil and gas industry which accounts for the largest share of the DAS market, requirements such as systems with a longer sensing range [9–11] and higher measurement accuracy [12–15]. Consequently, less effort has been directed towards improving the spatial resolution of DAS systems. With 1 m gauge length providing sufficient spatial resolution for DASs main target market, commercial DAS manufacturers have had little incentive to use shorter probe pulses to achieve sub-meter resolution by sacrificing the signal-to-noise ratio (SNR). This, in turn, has restricted the adoption of DAS technology in areas such as mechanical and civil engineering which require mapping dynamic strains with much higher resolution.

The most commonly used approach to obtain a high resolution map of dynamic strains along a structure is based on fibre Bragg grating (FBG) arrays [16, 17]. In this approach, several tens of FBGs with different Bragg wavelengths are used to measure strain levels at multiple points along the fibre. The number of sensing nodes in such an array, however, is usually limited to less than a hundred per fibre which may restrict the application of this approach. To address this limitation, sensing systems based on ultra-weak fibre Bragg grating (UWFBG) arrays have been developed [18–21]. UWFBG arrays, used in this approach, are comprised of several hundred low-reflectivity FBGs with an identical Bragg wavelength which, unlike conventional FBG arrays, are interrogated through time division multiplexing. Using this approach, Li et al. [22] have demonstrated a 2 km long sensing system based on an array of 960 UWFBGs with  $-40$  dB reflectivity capable of measuring dynamic strain with frequencies as high as 12.5 kHz. Despite exhibiting a superior strain accuracy, sensing systems that rely on UWFBG array are susceptible to signal fading due to slow drift in the Bragg wavelength of the FBGs as a result of localized temperature or strain changes. Any such drifts in the Bragg wavelength of the FBGs that pushes their reflection bands beyond the operating wavelength of the seed laser will result in signal fading.

45 Several studies have shown that DAS systems based on phase-sensitive optical time-domain  
46 reflectometry ( $\phi$ -OTDR) can achieve sub-meter spatial resolution by either sacrificing the  
47 sensitivity or using very high speed digitizers [23–26]. For instance, using 5 ns probe pulses,  
48 Masoudi et al. [23] have demonstrate a DAS system with 50 cm spatial resolution albeit with  
49 a minimum detectable strain amplitude of 40 n $\epsilon$  at 200 Hz. In 2018, Chen et al. [25] used a  
50 chirped-pulse  $\phi$ -OTDR to achieve 80 cm spatial resolution over 9.8 km sensing range. Although  
51 the setup achieved an excellent strain sensitivity of 245 p $\epsilon$ / $\sqrt{\text{Hz}}$ , it relied on a 2 GHz bandwidth  
52 oscilloscope and linear frequency modulation of up to 1 GHz to achieve a sub-meter spatial  
53 resolution. An extreme example of this approach was demonstrated by Martins et al. [26] where  
54 an oscilloscope with 62 GHz bandwidth was used to demonstrate a DAS with 2.5 cm spatial  
55 resolution. Although these examples show that  $\phi$ -OTDR can achieve sub-meter resolution  
56 along conventional telecom optical fibre, using high frequency electronics to achieve such high  
57 resolutions might be prohibitively expensive in many applications.

58 Other interrogation techniques such as optical frequency-domain reflectometry (OFDR) have  
59 also been used to obtain a high-resolution map of dynamic strains along sensing fibres [27–30].  
60 In this approach, the strain distribution along the sensing fibre is obtained by extracting the phase  
61 of the Rayleigh backscattered light from OFDR traces and calculating the changes in the value of  
62 the differential phase between adjacent points along the fibre. This interrogation technique has  
63 been used to demonstrate DAS with a spatial resolution as low as 10 cm over a sensing range of  
64 200 m. The main limitation of OFDR interrogation technique, however, is its trade-off between  
65 the measurement accuracy and spatial resolution [31].

66 Recently, a new class of specialty optical fibres has been developed that can enhance the  
67 backscattered signal by more than 20 dB above the naturally occurring Rayleigh backscattered  
68 signal. The enhancement in the intensity of the backscattered signal has been achieved by either  
69 forming a continuous grating along the fibre [32] or inscribing individual reflectors at fixed  
70 intervals in the core of the fibre [33]. In 2020, Zhang et al. [34] have shown that the spatial  
71 resolution of a conventional DAS system that operates based on  $\phi$ -OTDR interrogation technique  
72 can be reduced to as low as 20 cm if a continuous grating enhanced backscattering (CGEB) fibre  
73 is used as a sensing medium. In the following year, Xiong et al. [35] have used CGEB fibre to  
74 demonstrate a DAS system with 28 cm resolution, but over a much longer sensing range of up to  
75 920 m. Despite these successful demonstrations, since the intensity of the backscattered light in  
76 a CGEB fibre is proportional to the duration of the probe pulse, DAS systems based on CGEB  
77 fibre still encounter the same trade-off between the spatial resolution and SNR. Additionally,  
78 the enhancement in the intensity of the backscattered signal in CGEB fibre comes at the cost  
79 of higher attenuation level which, in turn, affects the sensing range of the sensor. Enhanced  
80 backscattering fibres based on point reflectors, on the other hand, does not suffer from the  
81 aforementioned trade-offs. This class of fibres, which are also known as ultra low-loss enhanced  
82 backscattering (ULEB) fibres, combines the advantages of UWFBG array and CGEB fibre to  
83 form a sensing medium that is capable of boosting the backscattered signal by more than 20 dB,  
84 has an extremely low excess loss (down to 0.01 dB excess loss per 100 reflectors [36]), and is  
85 wavelength independent. So far, ULEB fibres have been used to extend the sensing range and  
86 measurement precision of conventional DAS systems [36,37]. In this letter, a ULEB fibre with 50  
87 reflectors, spaced 10 cm apart, is used to demonstrate a high-resolution DAS based on  $\phi$ -OTDR  
88 interrogation technique. It is shown that such an arrangement can achieve a sensing range and  
89 measurement accuracy of 1 km and 1.9 n $\epsilon$ / $\sqrt{\text{Hz}}$ , respectively.

## 90 2. Principle

91 The sensing principle of the DAS setup, used in this study, is based on using a Mach-Zehnder  
92 interferometer (MZI) with a fixed path-imbalance to measure the phase difference between  
93 adjacent points along the sensing fibre. The role of the interferometer is to mix the backscattered

94 light from different points on the sensing fibre by splitting the backscattered signal into two  
 95 paths and combining them back with a fixed temporal delay. For an interferometer with a path  
 96 difference of  $\Delta L$ , the intensity at the output of the interferometer is given by [23]:

$$I = A + B \cos(\beta\Delta L + \Delta\Phi) \quad (1)$$

97 where  $\beta$  is the propagation constant of the probe pulse,  $\Delta\Phi$  is the phase difference between two  
 98 separate points on the fibre, and  $A$  and  $B$  are determined by the intensity of the backscattered light.  
 99 Since the gauge-length of the sensing arrangement, used in this study, is dictated by the spatial  
 100 separation between the reflectors in the ULEB fibre, the path-imbalance of the MZI should be  
 101 fixed to twice the distance between the reflectors. In order to avoid phase fading while extracting  
 102 the phase information from Eq. (1), a symmetric  $3 \times 3$  coupler can be used at the output of the  
 103 interferometer. The data from three arms of the  $3 \times 3$  coupler can then be combined to yield [38]:

$$\Delta\Phi = 0.78 \times \varepsilon \ell \frac{4\pi n}{\lambda} \quad (2)$$

104 where  $\varepsilon$  is the induced strain at a given section of the sensing fibre,  $\ell$  is the length of that section,  
 105  $n$  is the effective refractive index of the fibre, and  $\lambda$  is the wavelength of the seed laser. Equation  
 106 (2) shows that the phase-difference between the backscattered light from two adjacent reflectors  
 107 has a linear relationship with the induced strain between those reflectors.

### 108 3. Experiment

#### 109 3.1. Sensing Setup

110 The sensing arrangement is shown in Fig. 1. A narrow linewidth DFB laser diode ( $\lambda = 1550 \text{ nm}$ ,  
 111  $\Delta\nu = 100 \text{ kHz}$ ) is used as a seed laser. The laser output is intensity modulated by an electro-optic  
 112 modulator (EOM) to generate  $500 \text{ ps}$  probe pulses with  $25 \text{ kHz}$  repetition rate. To increase  
 113 the extinction ratio of the probe pulses, a semiconductor optical amplifier (SOA) is employed  
 114 as a pulse picker followed by a dense wavelength division multiplexing (DWDM) filter with  
 115  $100 \text{ GHz}$  bandwidth to limit the forward amplified spontaneous emission (ASE) of the SOA. As  
 116 a high-speed optical switch, the SOA plays an important role in generating a high extinction-ratio  
 117 probe pulse with short pedestal. The probe pulse with  $5 \text{ mW}$  peak power is launched into the  
 118 fibre under test (FUT) via circulator C1.

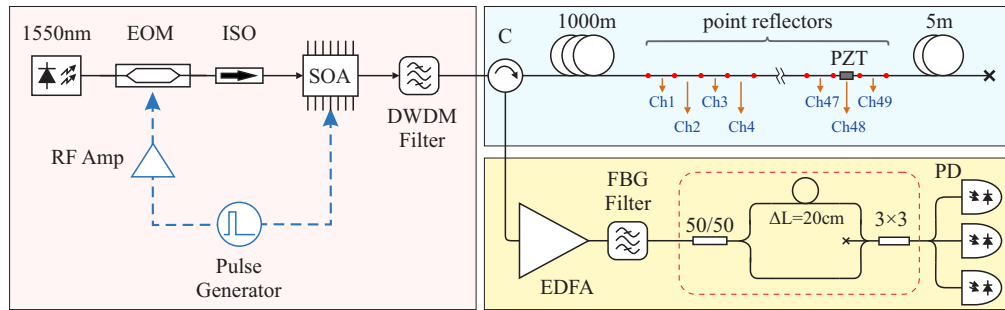


Fig. 1. Sensing setup of high-resolution DAS based on ULEB fibre. EOM: Electro-optic modulator; ISO: isolator; SOA: Semiconductor optical amplifier; DWDM: Dense wavelength division multiplexing; PZT: Piezo-electric actuator; C: Circulator; EDFA: Erbium-doped fibre amplifier; FBG: fibre Bragg grating; IMZI: Imbalanced Mach-Zehnder interferometer; PD: Photodetector; Data Acq.: Data acquisition unit. The red dots along the sensing fibre represent the point reflectors.

119 A 5 m long ULEB fibre with 50 point reflectors is spliced to 990 m long standard single-mode  
 120 fibre (SSMF) to form the FUT. A 50 mm long piezoelectric stacks (Thorlabs: PK4FXH3P2) is  
 121 attached to the ULEB fibre between its 48<sup>th</sup> and 49<sup>th</sup> reflectors, i.e. the second to last channel of  
 122 the ULEB fibre, to generate test signals. An extra 5 m of SSMF is added after the ULEB fibre to  
 123 separate it from the far-end of the FUT.

124 At the receiving arm of the sensing system, the backscattered signal from the FUT is  
 125 first amplified by an Erbium-doped optical amplifier (EDFA) and filtered by an FBG filter  
 126 ( $\lambda_B = 1550.1 \text{ nm}$ ,  $\Delta\lambda = 0.2 \text{ nm}$ , Reflectivity = 99%) to minimize the ASE. The amplified  
 127 backscattered light is then passed through a MZI with 20 cm path imbalance to mix the  
 128 back-reflected signals from adjacent reflectors. Finally, the mixed signal at the output of the  
 129 interferometer is detected by three amplified photodetectors ( $BW = 600 \text{ MHz}$ ,  $TIA = 40 \text{ k}\Omega$ )  
 130 and sampled with a 500 MHz bandwidth PCIe digitizer at a rate of 1.25 GS/s. The captured  
 131 data is then analyzed using Arctan demodulation algorithm [23] to extract the phase information.

### 132 3.2. ULEB Fibre Inscription Setup

133 The ULEB fibre, used in this test, was fabricated using an automated reel-to-reel fibre inscription  
 134 setup, a schematic of which is shown in Fig. 2(a). An objective lens was used to focus the output  
 135 of a femtosecond laser with pulse duration and energy of 200 fs and 4  $\mu\text{J}$ , respectively, on the  
 136 target fibre. Data from a CCD camera was used to automatically align the fibre at the focal point  
 137 of the objective lens using a multi-axis stage. A pulley arrangement was used to control the fibre  
 138 tension during the inscription procedure. An *in-situ* OTDR system was used to allow measuring  
 139 the optical signal during inscription. This allowed to control the reflectivity level at each reflector  
 140 and achieve a consistency of  $\pm 2 \text{ dB}$ .

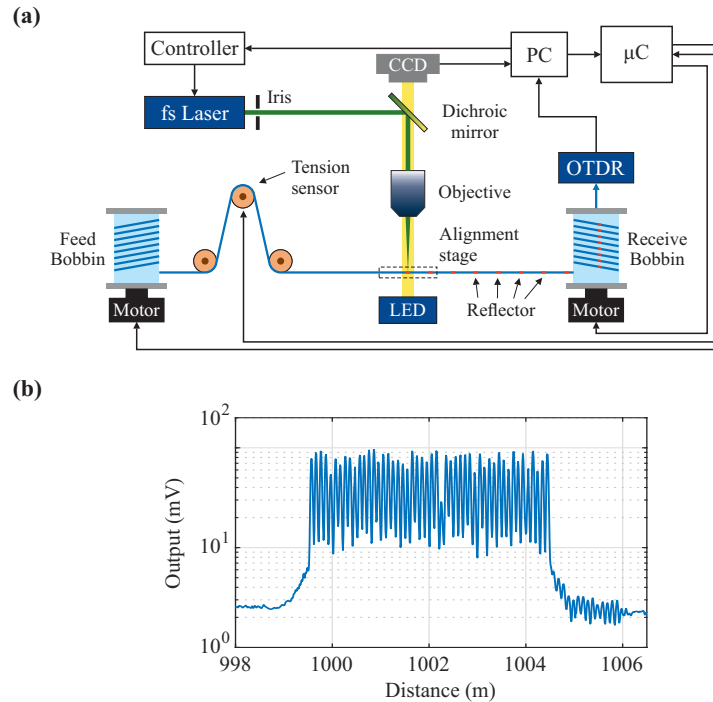


Fig. 2. (a) Schematic of the reel-to-reel, automated, fibre inscription set up. (b) The OTDR trace of the ULEB fibre at the far-end of the FUT exhibiting 50 reflectors with an average reflectivity of 14 dB above the intensity of the Rayleigh backscattered light.

141 The inscription setup was used to write 50 point reflectors with an average reflectance of  
 142  $-56\text{ dB}$  and a spatial separation of  $10\text{ cm}$  in the core of a SSMF through its polymer coating.  
 143 With each pair of reflectors constituting a single sensing channel, the ULEB fibre, used in this  
 144 test, had 49 measurement channels. With an inscription speed of under 2 minutes per reflector  
 145 which includes fibre alignment, reflector inscription, and rewinding, the number of reflectors  
 146 used for this study was reduced to 50 to keep the fibre fabrication time under 2 hours.

#### 147 4. Results and Discussion

148 Figure 2(b) shows the OTDR trace of the ULEB fibre at the far-end of the FUT. All 50 reflectors  
 149 with an average reflectance of  $-56\text{ dB}$  can be seen in this diagram. 98% of the reflectors exhibited  
 150 a relatively uniform reflectivity with less than  $3\text{ dB}$  variation. Only one reflector had lower than  
 151 expected reflectance (28<sup>th</sup> reflector with  $-60\text{ dB}$  reflectance). The oscillation in the OTDR trace  
 152 that occurs after the reflectors over the spatial interval of  $1005\text{ m} - 1006\text{ m}$  can be linked to the  
 153 pedestal of the probe pulse. Since electrical pulses applied to the SOA for pulse picking were  
 154  $10\text{ ns}$  long, limited by the speed of the pulse generator, the optical pulses used for interrogating  
 155 the FUT had  $9.5\text{ ns}$  pedestal. Despite  $25\text{ dB}$  extinction ratio between the main optical pulse and  
 156 its pedestal, the interaction between  $95\text{ cm}$  pedestal and 9 reflectors give rise to the oscillatory  
 157 pattern on the OTDR trace.

158 Figure 3(a) shows the waterfall diagram of the sensing system at the far-end of the sensing  
 159 fibre. The location and profile of a  $30\text{ Hz}$  vibration, which was used as the test signal, can be  
 160 clearly identified at  $L = 1004\text{ m}$  on the diagram. The color bar on the diagram indicates the  
 161 strain level imposed on the fibre in  $\mu\epsilon$ . The fast Fourier transform (FFT) of the strain level along  
 162 the FUT is shown in the spectrogram of Fig. 3(b). The  $30\text{ Hz}$  modulation at  $1004.9\text{ m}$  with peak  
 163 strain level of  $29.3\mu\epsilon$  can be identified on this diagram.

164 Fig. 4(a) shows a 2D cross-section of the waterfall diagram at a fixed location on the FUT,  
 165 corresponding to the 48<sup>th</sup> channel of the ULEB fibre, as a function of time. In order to quantify  
 166 the spatial resolution of the sensor, a 2D cross-section of the spectrogram at  $f = 30\text{ Hz}$ , is shown  
 167 in Fig. 4(b). The rising edge of the strain profile, shown in this plot, is  $8\text{ cm}$  which is less than  
 168 the  $10\text{ cm}$  spatial resolution of the system dictated by the spacing between the reflectors. This

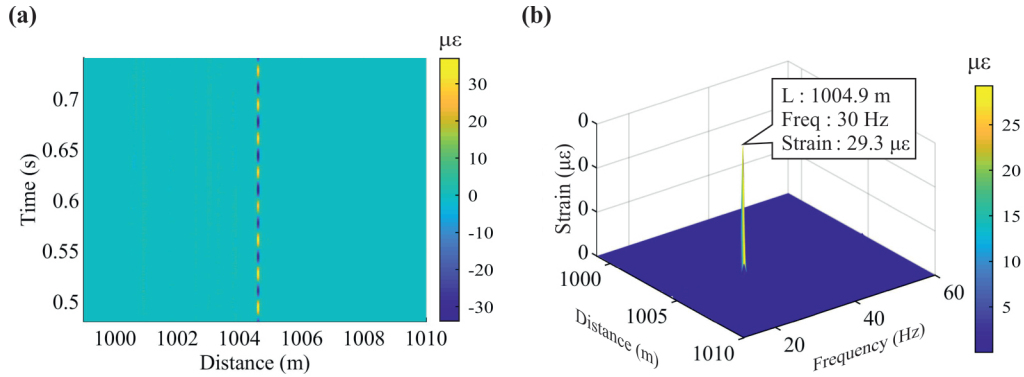


Fig. 3. a) Waterfall plot of the sensing system at the far end of the sensing fibre. The horizontal axis represents the distance along the sensing fibre while the vertical axis represents the elapsed time. b) Spectrogram of the system output mapping strain level at the last  $25\text{ m}$  of the FUT as a function of frequency. c) 2D cross-section of the waterfall plot showing the strain variation at the the 48<sup>th</sup> channel of the ULEB fibre as a function of time. d) 2D cross-section of the spectrogram plot, taken perpendicular to the frequency axis at  $f = 30\text{ Hz}$ , demonstrating the spatial resolution of the system.

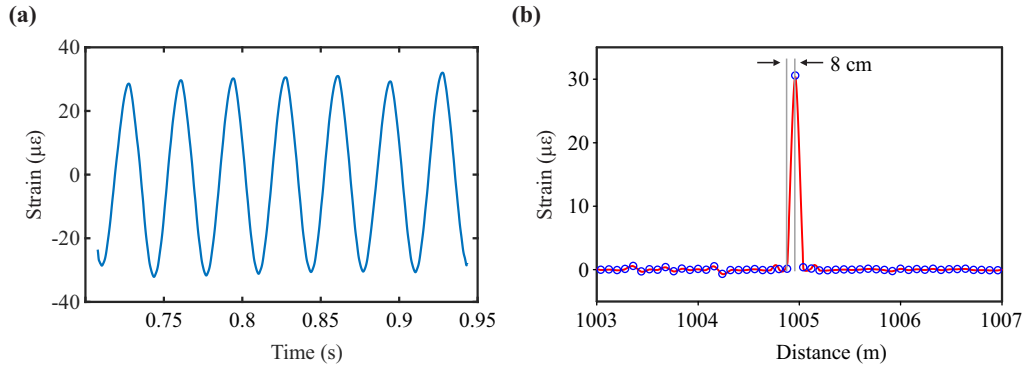


Fig. 4. a) 2D cross-section of the waterfall plot showing the strain variation at the the 48<sup>th</sup> channel of the ULEB fibre as a function of time. b) 2D cross-section of the spectrogram plot, taken perpendicular to the frequency axis at  $f = 30 \text{ Hz}$ , demonstrating the spatial resolution of the system.

169 discrepancy is due to the mismatch between the sampling rate of the digitizer that is used to  
 170 capture the backscattered light and the spacing between the reflectors along the ULEB fibre.  
 171 With  $1.25 \text{ GS/s}$  sampling rate, the digitizer acquire one sample every  $8 \text{ cm}$ . Hence, the rise time of  
 172 the signal appears to be less than the  $10 \text{ cm}$  spacing between the reflectors.

173 In order to assess the noise floor and cross-talk of the sensing arrangement, amplitude spectral  
 174 densities (ASDs) of the strain levels at the last three channels of the ULEB fibre are shown in Fig.  
 175 5(a). The ASD of the strain level at the 48<sup>th</sup> channel of the ULEB fibre, the channel which is  
 176 stimulated by the PZT actuator, is represented by the blue trace. The peak at  $30 \text{ Hz}$  shows the  
 177 frequency and amplitude of the test signal. The yellow trace shows the ASD of the strain at the  
 178 47<sup>th</sup> channel of the ULEB fibre, a sensing channel before the PZT that has not been disturbed.  
 179 The noise floor of the system, calculated by averaging the noise from  $10 \text{ Hz}$  to  $1 \text{ kHz}$ , shows a  
 180 phase noise of  $-29.23 \text{ (re rad}/\sqrt{\text{Hz}})$  which corresponds to a strain noise of  $1.9 \text{ n}\epsilon/\sqrt{\text{Hz}}$ . The  
 181 noise floor is identified by the dashed line on the figure. To assess the cross-talk between the  
 182 adjacent sensing channels, the ASD of the 48<sup>th</sup> channel (the channel attached to the PZT) is  
 183 compared with that of the 49<sup>th</sup> channel which is represented by the red trace on the plot. The  
 184 analysis of the frequency peaks on the two traces shows a cross-talk of less than  $21 \text{ dB}$ . With  
 185 an excess loss of  $0.01 \text{ dB}$  per 100 reflectors, our analysis shows that replacing the SSMF at the  
 186 front-end of the FUT with ULEB fibre with  $10 \text{ cm}$  spacing will not have any notable impact  
 187 on the noise and cross-talk levels of the sensing system. With previous studies showing the  
 188 capability of DAS system in measuring  $33 \text{ n}\epsilon/\sqrt{\text{Hz}}$  vibration along a ULEB fibre at the far-end  
 189 of  $152 \text{ km}$  SSMF with total round-trip loss of  $60 \text{ dB}$  [37],  $1 \text{ dB}$  excess loss from  $1 \text{ km}$  long ULEB  
 190 fibre with  $10 \text{ cm}$  spacing will have no substantial effect on the sensitivity of the system.

191 The intra-channel noise and inter-channel cross-talk, observed in the result, can be associated  
 192 with the pedestal of the probe pulse as discussed earlier. The interaction of the pedestal with other  
 193 reflectors along the ULEB fibre causes additional light reflection which gets added to the reflected  
 194 light from the main pulse and causes distortion. Hence, by reducing the duration of pulse picking  
 195 signal to better match the width of the probe pulse, it is possible to significantly reduce both  
 196 the noise floor of the system and the cross-talk between different channels. Additionally, the  
 197 mismatch between the sampling rate of the digitizer and the spatial resolution of the sensing fibre  
 198 may contribute to the overall noise floor of each sensing channel.

199 In order to assess the linearity of the system, the sensing setup was used to measure the strain  
 200 level at channel 48 of the ULEB fibre while increasing the drive voltage applied to the PZT  
 201 from  $0.5 \text{ V}$  to  $20 \text{ V}$ . The measurements, represented by blue circles in Fig. 5(b), exhibited a

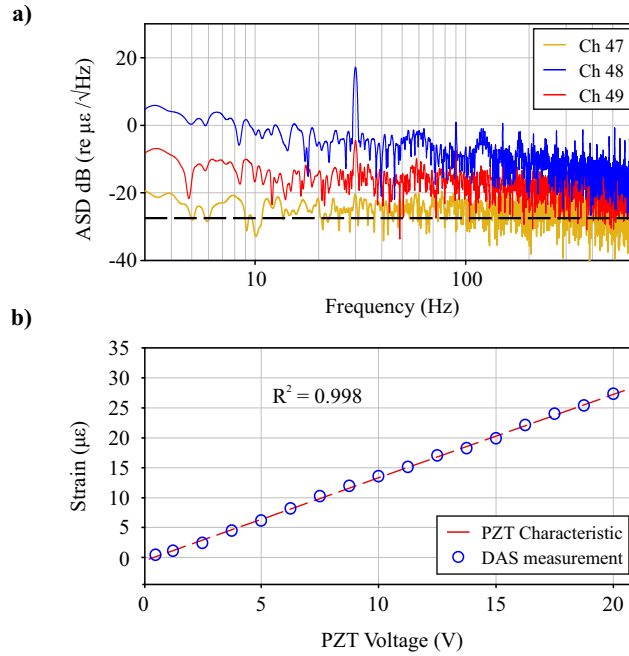


Fig. 5. a) Amplitude spectral density (ASD) of the strain levels at the last three channels of the ULEB fibre. The blue trace represents the ASD of the strain level at the 48<sup>th</sup> sensing channel where the PZT actuator is located. The yellow and red traces represent the ASD of the strain level at 47<sup>th</sup> and 49<sup>th</sup> channels of the ULEB fibre, respectively, i.e. the sensing channels just before and just after the PZT. The dashed line at the bottom of the plot represents the noise floor of the sensor. b) The peak strain level measured by the DAS system (blue circles) for 30 Hz sinusoidal test signals at various amplitudes from 0.5 V to 20 V. The red dashed line represents the response of the PZT transducer, characterised separately with a Michelson interferometer.

202 high correlation ( $R^2 = 0.998$ ) with the response of the PZT transducer which was characterized  
 203 separately using a Michelson interferometer (dashed red line). In addition, the response of the  
 204 system to vibrations across a wide frequency range from 0.1 Hz to 5 kHz was assessed confirming  
 205 the linear response of the sensing arrangement.

## 206 5. Conclusion

207 In summary, a high resolution DAS system based on ULEB fibre is demonstrated. It is shown that,  
 208 unlike conventional sensing systems that are based on SSMF or CGEB fibres, the DAS systems  
 209 that use ULEB fibre as a sensing medium do not experience the trade-off between the spatial  
 210 resolution and SNR. A ULEB fibre with 50 reflectors and an average reflectance of  $-56$  dB is  
 211 used to demonstrate a DAS with 10 cm spatial resolution at the far-end of 1 km sensing fibre. To  
 212 fabricate a ULEB fibre with consistent reflectivity, an automated reel-to-reel fibre inscription  
 213 setup with an *in-situ* OTDR feedback system is developed. A simple sensing arrangement based  
 214 on a digitizer with 600 MHz bandwidth and an imbalanced MZI is used to achieve this resolution.

215 The sensor exhibited a high degree of linearity, a  $1.9$   $n\epsilon/\sqrt{\text{Hz}}$  ASD noise floor, and a maximum  
 216 channel cross-talk of less than 21 dB. The spatial resolution of the measurement, achieved in this  
 217 work, was limited by the sampling rate and bandwidth of the digitizer. Using a digitizer with  
 218 3 GHz bandwidth and 100 ps probe pulse with sech-squared profile, it is possible to push the  
 219 spatial resolution of ULEB-based DAS to as low as 1 cm.

220 **Funding.** Royal Society (CHL/R1/180350); Natural Environment Research Council (NE/S012877/1,  
221 NE/T005890/1); Royal Academy of Engineering (PoC1920/21, RF1415/14/6).

222 **Disclosures.** The authors declare no conflicts of interest.

223 **Acknowledgements.** For the purpose of open access, the author has applied a creative commons attribution  
224 (CC BY) licence (where permitted by UKRI, ‘open government licence’ or ‘creative commons attribution  
225 no-derivatives (CC BY-ND) licence’ may be stated instead) to any author accepted manuscript version  
226 arising.

227 **Data availability.** Openly available at 10.5258/SOTON/D2116.

## 228 References

- 229 1. D. Molteni, M. J. Williams, and C. Wilson, “Detecting microseismicity using distributed vibration,” *First Break*. **35**  
230 (2017).
- 231 2. P. Jousset, T. Reinsch, T. Ryberg, H. Blanck, A. Clarke, R. Aghayev, G. P. Hersir, J. Hennings, M. Weber, and C. M.  
232 Krawczyk, “Dynamic strain determination using fibre-optic cables allows imaging of seismological and structural  
233 features,” *Nat. Commun.* **9**, 1–11 (2018).
- 234 3. N. J. Lindsey and E. R. Martin, “Fiber-optic seismology,” *Annu. Rev. Earth Planet. Sci.* **49**, 309–336 (2021).
- 235 4. D. Milne, A. Masoudi, E. Ferro, G. Watson, and L. Le Pen, “An analysis of railway track behaviour based on  
236 distributed optical fibre acoustic sensing,” *Mech. Syst. Signal Process.* **142**, 106769 (2020).
- 237 5. A. Mateeva, J. Lopez, H. Potters, J. Mestayer, B. Cox, D. Kiyashchenko, P. Wills, S. Grandi, K. Hornman,  
238 B. Kuvshinov *et al.*, “Distributed acoustic sensing for reservoir monitoring with vertical seismic profiling,” *Geophys.*  
239 *Prospect.* **62**, 679–692 (2014).
- 240 6. A. Lellouch and B. L. Biondi, “Seismic applications of downhole das,” *Sensors* **21**, 2897 (2021).
- 241 7. A. Masoudi, J. A. Pilgrim, T. P. Newson, and G. Brambilla, “Subsea cable condition monitoring with distributed  
242 optical fiber vibration sensor,” *J. Light. Technol.* **37**, 1352–1358 (2019).
- 243 8. Z. W. Ding, X. P. Zhang, N. M. Zou, F. Xiong, J. Y. Song, X. Fang, F. Wang, and Y. X. Zhang, “Phi-OTDR based  
244 on-line monitoring of overhead power transmission line,” *J. Light. Technol.* **39**, 5163–5169 (2021).
- 245 9. L. D. Van Putten, A. Masoudi, and G. Brambilla, “100-km-sensing-range single-ended distributed vibration sensor  
246 based on remotely pumped erbium-doped fiber amplifier,” *Opt. Lett.* **44**, 5925–5928 (2019).
- 247 10. S. Liehr, C. Borchardt, and S. Münzenberger, “Long-distance fiber optic vibration sensing using convolutional neural  
248 networks as real-time denoisers,” *Opt. Express* **28**, 39311–39325 (2020).
- 249 11. O. H. Waagaard, E. Rønnekleiv, A. Haukanes, F. Stabo-Eeg, D. Thingbø, S. Forbord, S. E. Aasen, and J. K. Brenne,  
250 “Real-time low noise distributed acoustic sensing in 171 km low loss fiber,” *OSA Continuum* **4**, 688–701 (2021).
- 251 12. A. Hartog, L. Liokumovich, N. Ushakov, O. Kotov, T. Dean, T. Cuny, A. Constantinou, and F. Englich, “The use of  
252 multi-frequency acquisition to significantly improve the quality of fibre-optic-distributed vibration sensing,” *Geophys.*  
253 *Prospect.* **66**, 192–202 (2018).
- 254 13. Z. Ju, Z. Yu, Q. Hou, K. Lou, M. Chen, Y. Lu, and Z. Meng, “Low-noise and high-sensitivity  $\phi$ -OTDR based on an  
255 optimized dual-pulse heterodyne detection scheme,” *Appl. Opt.* **59**, 1864–1870 (2020).
- 256 14. Y. Wakisaka, D. Iida, H. Oshida, and N. Honda, “Fading suppression of  $\phi$ -OTDR with the new signal processing  
257 methodology of complex vectors across time and frequency domains,” *J. Light. Technol.* (2021).
- 258 15. H. M. Ogden, M. J. Murray, J. B. Murray, C. Kirkendall, and B. Redding, “Frequency multiplexed coherent  $\varphi$ -OTDR,”  
259 *Sci. Reports* **11**, 1–12 (2021).
- 260 16. P. Shrestha, J. H. Kim, Y. Park, and C.-G. Kim, “Impact localization on composite wing using 1D array FBG sensor  
261 and rms/correlation based reference database algorithm,” *Compos. Struct.* **125**, 159–169 (2015).
- 262 17. H. Alexakis, F. D. H. Lau, and M. J. DeJong, “Fibre optic sensing of ageing railway infrastructure enhanced with  
263 statistical shape analysis,” *J. Civ. Struct. Heal. Monit.* **11**, 49–67 (2021).
- 264 18. F. Zhu, Y. Zhang, L. Xia, X. Wu, and X. Zhang, “Improved  $\phi$ -OTDR sensing system for high-precision dynamic  
265 strain measurement based on ultra-weak fiber Bragg grating array,” *J. Light. Technol.* **33**, 4775–4780 (2015).
- 266 19. Y. Wang, P. Lu, S. Mihailov, L. Chen, and X. Bao, “Strain measurement range enhanced chirped pulse  $\varphi$ -OTDR for  
267 distributed static and dynamic strain measurement based on random fiber grating array,” *Opt. Lett.* **45**, 6110–6113  
268 (2020).
- 269 20. C. Li, J. Tang, Y. Jiang, C. Cheng, L. Cai, and M. Yang, “An enhanced distributed acoustic sensor with large  
270 temperature tolerance based on ultra-weak fiber Bragg grating array,” *IEEE Photonics J.* **12**, 1–11 (2020).
- 271 21. C. Li, J. Tang, C. Cheng, L. Cai, and M. Yang, “FBG arrays for quasi-distributed sensing: A review,” *Photonic*  
272 *Sensors* **11**, 91–108 (2021).
- 273 22. Z. Li, Y. Tong, X. Fu, J. Wang, Q. Guo, H. Yu, and X. Bao, “Simultaneous distributed static and dynamic sensing  
274 based on ultra-short fiber Bragg gratings,” *Opt. Express* **26**, 17437–17446 (2018).
- 275 23. A. Masoudi and T. P. Newson, “High spatial resolution distributed optical fiber dynamic strain sensor with enhanced  
276 frequency and strain resolution,” *Opt. Lett.* **42**, 290–293 (2017).
- 277 24. S. Feng, T. Xu, J. Huang, Y. Yang, L. Ma, and F. Li, “Sub-meter spatial resolution phase-sensitive optical time-domain  
278 reflectometry system using double interferometers,” *Appl. Sci.* **8**, 1899 (2018).



- 279 25. D. Chen, Q. Liu, and Z. He, "High-fidelity distributed fiber-optic acoustic sensor with fading noise suppressed and  
280 sub-meter spatial resolution," *Opt. Express* **26**, 16138–16146 (2018).
- 281 26. H. Martins, K. Shi, B. Thomsen, S. Martin Lopez, M. Gonzalez Herraes, and S. Savory, "Real time dynamic strain  
282 monitoring of optical links using the backreflection of live PSK data," *Opt. Express* **24**, 22303–22318 (2016).
- 283 27. D. Arbel and A. Eyal, "Dynamic optical frequency domain reflectometry," *Opt. Express* **22**, 8823–8830 (2014).
- 284 28. J. Li, J. Gan, Z. Zhang, X. Heng, C. Yang, Q. Qian, S. Xu, and Z. Yang, "High spatial resolution distributed fiber  
285 strain sensor based on phase-OFDR," *Opt. Express* **25**, 27913–27922 (2017).
- 286 29. L. Marcon, A. Galtarossa, and L. Palmieri, "High-frequency high-resolution distributed acoustic sensing by optical  
287 frequency domain reflectometry," *Opt. Express* **27**, 13923–13933 (2019).
- 288 30. H. Li, Q. Liu, D. Chen, Y. Deng, and Z. He, "High-spatial-resolution fiber-optic distributed acoustic sensor based on  
289  $\phi$ -OFDR with enhanced crosstalk suppression," *Opt. Lett.* **45**, 563–566 (2020).
- 290 31. C. Liang, Q. Bai, M. Yan, Y. Wang, H. Zhang, and B. Jin, "A comprehensive study of optical frequency domain  
291 reflectometry," *IEEE Access* **9**, 41647–41668 (2021).
- 292 32. P. S. Westbrook, K. S. Feder, T. Kremp, E. M. Monberg, H. Wu, B. Zhu, L. Huang, D. A. Simoff, S. Shenk, V. A.  
293 Handerek *et al.*, "Enhanced optical fiber for distributed acoustic sensing beyond the limits of Rayleigh backscattering,"  
294 *IScience* **23**, 101137 (2020).
- 295 33. A. Donko, R. Sandoghchi, A. Masoudi, M. Beresna, and G. Brambilla, "Surpassing the detection limits of current  
296 distributed acoustic sensing systems," in *26th International Conference on Optical Fiber Sensor*, (OSA, 2018). Paper  
297 WF75.
- 298 34. L. Zhang, Z. Yang, N. Gorbatov, R. Davidi, M. Galal, L. Thévenaz, and M. Tur, "Distributed and dynamic strain  
299 sensing with high spatial resolution and large measurable strain range," *Opt. Lett.* **45**, 5020–5023 (2020).
- 300 35. J. Xiong, Z. Wang, J. Jiang, B. Han, and Y. Rao, "High sensitivity and large measurable range distributed acoustic  
301 sensing with Rayleigh-enhanced fiber," *Opt. Lett.* **46**, 2569–2572 (2021).
- 302 36. B. Redding, M. J. Murray, A. Donko, M. Beresna, A. Masoudi, and G. Brambilla, "Low-noise distributed acoustic  
303 sensing using enhanced backscattering fiber with ultra-low-loss point reflectors," *Opt. Express* **28**, 14638–14647  
304 (2020).
- 305 37. A. Masoudi, M. Beresna, and G. Brambilla, "152 km-range single-ended distributed acoustic sensor based on inline  
306 optical amplification and a micromachined enhanced-backscattering fiber," *Opt. Lett.* **46**, 552–555 (2021).
- 307 38. L. D. van Putten, A. Masoudi, J. Snook, and G. Brambilla, "Numerical modelling of a distributed acoustic sensor  
308 based on ultra-low loss-enhanced backscattering fibers," *Sensors* **21**, 6869 (2021).